Available online at www.sciencedirect.com
SCIENCE DIRECT®
Computers and Structures 82 (2004) 1793–1804
Computers & Structures
www.elsevier.com/locate/compstruc

Scattering of seismic waves generated by an irregular seabed

Paulo Santos *, António Tadeu

Department of Civil Engineering, University of Coimbra, Polo II, Coimbra 3030-290, Portugal

Received 19 May 2003; accepted 6 May 2004
Available online 3 July 2004

Abstract

The changes in the seismic response due to the presence of an irregular elastic seabed, and/or the presence of a water-filled inclusion located under the elastic seabed surface, in the presence of a dilatational spatially harmonic line source, is assessed. The seabed surface deformations and the water-filled inclusions are bi-dimensional.

The solution is obtained using the Boundary Elements Method for a wide range of frequencies and spatially harmonic line sources, which are then used to compute the time series by means of fast inverse Fourier transforms.

Keywords: Boundary elements; Seabed irregularities; Seismic wave amplification

1. Introduction

The amplification and de-amplification of seismic signals caused by heterogeneities near the surface has been studied for many years. Some of the earlier studies report the use of analytical solutions to look at the scattering and diffraction produced by alluvial basins of regular shape [1] and the wave scattering caused by cavities [2]. Semi-analytical methods have been used to examine the diffraction of waves by geological inclusions with arbitrary cross-sections placed in a homogeneous medium [3–5]. Numerical methods, such as finite elements and differences, have been used to determine the response within localized, irregular domains, such as the study of soil structure interaction [6,7]. Discrete methods have also occasionally been used to model large alluvial basins, but only in plane-strain [8]. The BEM has recently been applied by Stamos and Beskos [9], to a problem where long, lined tunnels, with a uniform cross-section, were buried in a half-space. These authors described the three-dimensional (3D) dynamic response to plane harmonic waves, propagating in several directions, by treating it as a series of two-dimensional (2D) problems.

The existence of topographic irregularities can also influence the seismic response. Pedersen et al. [10] used the IBEM to analyze the 3D seismic response of 2D topographic features to plane waves, employing Green's functions for a harmonic point force moving along the axis of the topography in a full space. They give results in the frequency and time domains for topographical deformations with simple geometry, such as a semi-circular canyon or a semi-circular ridge, subjected to incident plane waves.

More recently Santos et al. [11] have studied the 3D scattering field obtained when 2D smooth topographical deformations are subjected to a dilatational point load located inside the elastic half-space, using the Boundary Elements Method. These authors applied the same method to study the influence of a cavity, located near the half-space surface, on the seismic amplifications [12].

Semblat et al. [13] compared the BEM results for the analysis of seismic wave amplification with experimental findings. They concluded that the thickness of the surface layer, its mechanical properties, its general shape, and the seismic wave type involved have a considerable influence on amplification and the frequency at which it occurs. Dineva and Manolis [14] used the Boundary Integral Equation Method to evaluate the scattering of

* Corresponding author. Tel.: +351-239-797201; fax: +351-239-797190.
E-mail address: pfsantos@dec.uc.pt (P. Santos).

0045-7949/$ - see front matter
doi:10.1016/j.compstruc.2004.05.003

seismic waves by cracks in multi-layered geological regions.

In the context of oceans, authors have formulated different models for studying the solid–fluid interactions induced at the seabed. Dawson and Fawcett [15] studied the scattering of underwater sound by irregularities of an oceanic waveguide surface, using the Boundary Integral Equation Method. In his numerical examples, the fluid filling the waveguide is assumed to have constant density and sound speed. However, the solution involves a Green's function appropriate for a waveguide with a flat surface, which allows the sound speed to vary with depth. Godinho et al. [16] used the BEM to evaluate the 3D acoustic scattering from an irregular fluid waveguide. In papers [15,16], referred to above, the floor of the waveguide was considered to be rigid, while the fluid surface was assumed to be free. Ingenito [17] developed theoretical expressions for the acoustic field scattered by a rigid sphere submerged in a fluid layer overlying a horizontally stratified elastic medium. Makris [18] developed a spectral formulation for handling the scattering generated by a 3D object in layered media, and applied it to submerged spheres. This formulation is valid when the source and receiver are far enough away from the object for multiple scattering between the object and the waveguide boundaries to be disregarded.

In this work the BEM is used to model the 3D seismic response of an elastic seabed. The surface of the seabed is first modeled as flat and the results are then compared with those for a seabed which has smooth 2D deformations. The alteration of the seismic response due to the introduction of a circular cylindrical water-filled inclusion below the seabed surface is also analyzed.

First, the formulation of the problem for an elastic seabed subjected to a dilatational point source is presented. The method for achieving the results in the time domain is explained. The results given by numerical applications are then presented, and the influences of the seabed surface deformations, and the presence of water-filled inclusions, in the seismic response, are analyzed. Finally, some concluding remarks are presented.

2. The problem

A fluid-filled inclusion is driven along the z direction in an elastic seabed, allowing a shear wave velocity of β and a compressional wave velocity of α , with density ρ (see Fig. 1). The fluid medium has density ρ_f and permits a compressional wave velocity α_f. A dilatational point source is placed in the elastic medium at position (x_0, y_0, z_0) , oscillating with a frequency ω. The incident field can be expressed by the dilatational potential ϕ:

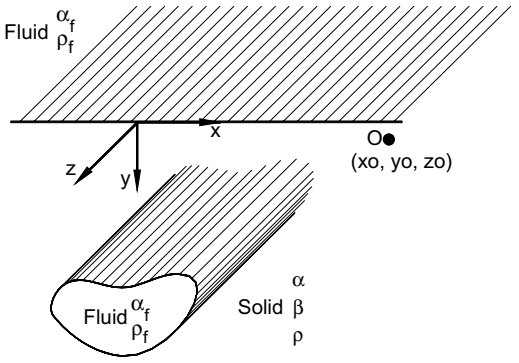

Fig. 1. Geometry of the problem.

$$\phi_{\text{inc}} = \frac{A e^{i\omega\left(\alpha t - \sqrt{(x-x_0)^2+(y-y_0)^2+(z-z_0)^2}\right)}}{\sqrt{(x-x_0)^2+(y-y_0)^2+(z-z_0)^2}} \tag{1}$$

in which A is the wave amplitude; t denotes time and $i = \sqrt{-1}$.

This problem can be solved as a summation of two-dimensional problems, for varying effective wavenumbers [19],

$$k_\alpha = \sqrt{\frac{\omega^2}{\alpha^2} - k_z^2}, \quad \operatorname{Im} k_\alpha < 0 \tag{2}$$

where k_z is the axial wavenumber after Fourier transformation of the problem in the z direction. The incident field in this frequency wavenumber domain is given by

$$\hat{\phi}_{\text{inc}}(\omega, x, y, k_z) = \frac{-iA}{2} H_0^{(2)}\left(k_\alpha \sqrt{(x-x_0)^2+(y-y_0)^2}\right) \tag{3}$$

in which the $H_n^{(2)}(\cdots)$ are second Hankel functions of order n.

3. BEM solution

The BEM is used to find the solution of a cylindrical fluid-filled inclusion in an elastic unbounded medium, subjected to a wave field generated by a point blast source, by discretizing only its boundary. The BEM equations that are applied to this problem are well known (see [20,21]). The system of equations required for the solution is arranged so as to impose the continuity of the normal displacements and normal stresses and null shear stresses along the boundary of the fluid-filled inclusion. This system of equations requires the evaluation of the following integrals along the appropriately discretized boundary of the inclusion

$$H_{ij}^{(s)kl} = \int_{C_l} H_{ij}^{(s)}(x_k, x_l, n_l)\,\mathrm{d}C_l \quad (i,j = 1,2,3)$$

$$H_{f1}^{(f)kl} = \int_{C_l} H_{f1}^{(f)}(x_k, x_l, n_l)\,\mathrm{d}C_l$$

$$G_{ij}^{(s)kl} = \int_{C_l} G_{ij}^{(s)}(x_k, x_l)\,\mathrm{d}C_l \quad (i = 1,2,3;\ j = 1)$$

$$G_{f1}^{(f)kl} = \int_{C_l} G_{f1}^{(f)}(x_k, x_l)\,\mathrm{d}C_l \tag{4}$$

in which $H_{ij}^{(s)}(x_k, x_l, n_l)$ and $G_{ij}^{(s)}(x_k, x_l)$ are, respectively, the Green's tensor for traction and displacement components in the elastic medium, at point x_l in direction j, caused by a concentrated load acting at the source point x_k in direction i; $H_{f1}^{(f)}(x_k, x_l, n_l)$ are the components of the Green's tensor for pressure in the fluid medium, at point x_l caused by a pressure load acting at the source point x_k; $G_{f1}^{(f)}(x_k, x_l)$ are the components of the Green's tensor for displacement in the fluid medium, at point x_l in the normal direction, caused by a pressure load acting at the source point x_k; n_l is the unit outward normal for the lth boundary segment C_l ; the subscripts $i, j = 1,2,3$ denote the normal, tangential and z directions, respectively. These equations are conveniently transformed from the x, y, z Cartesian coordinate system by means of standard vector transformation operators. The required two-and-a-half-dimensional fundamental solution (Green's functions) and stress functions in Cartesian co-ordinates, for the elastic and fluid media, can be found in [22].

The required integrations in Eq. (4) are performed analytically for the loaded element [23,24], and using a Gaussian quadrature scheme when the element to be integrated is not the loaded element. The BEM algorithm was implemented and validated by applying it to a cylindrical circular borehole filled with an inviscid fluid, for which the solution is known in closed form (see [25]).

The equations developed for the fluid-filled inclusion (Eq. (4)), can be used to calculate the solution for a seabed interface subjected to a seismic wave field because the boundary conditions are of the same type. The use of complex frequencies together with the geometrical damping of the response with distance makes the full discretization of the infinite surface unnecessary. Boundary elements are only required to the extent that they make a significant contribution to the response. If solutions are required in the time domain, the contribution to the response behind the numerical time window, defined by the frequency step ($\Delta\omega$) of the analysis, $T = 2\pi/\Delta\omega$, need not be taken into account. Hence, the boundary elements are distributed along the surface up to a distance (L_{dist}) from the receivers, given by $L_{\mathrm{dist}} = \alpha T$. This gives a discretized surface with length $2L_{\mathrm{dist}} + 2a$, where $2a$ is the length of the segment occupied by the receivers (Fig. 2). Many simulations were performed to study how varying the size of boundary elements affects the accuracy of the response. The

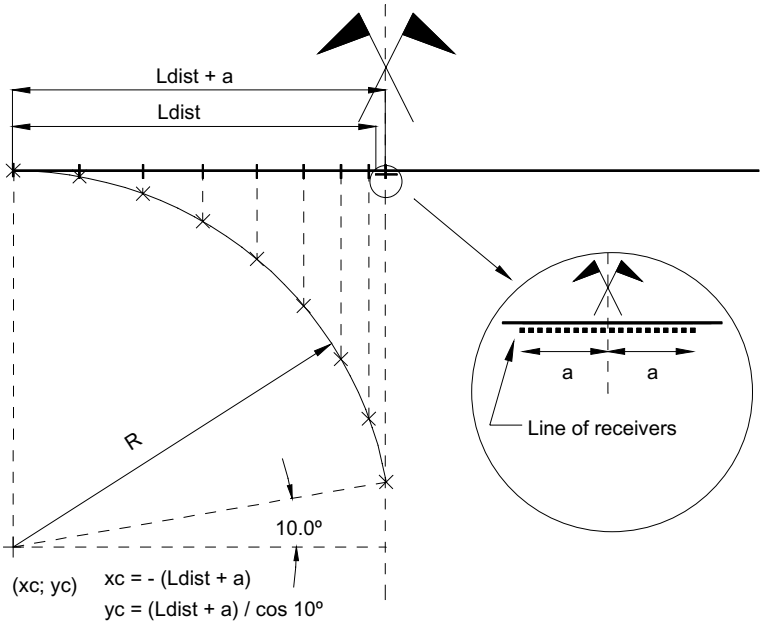

Fig. 2. Boundary elements distribution along the seabed surface.

performance was found to be better when smaller elements were placed in the vicinity of the receivers. The scheme used in this work to define the size of the boundary elements is illustrated in Fig. 2. The authors of this paper suggest that boundary elements of varying size should be placed along the surface, with the shorter elements being used nearer to the center of the surface boundary discretization, thereby reducing computational cost.

The BEM algorithm was implemented and validated by applying it to a flat solid–fluid interface (with no inclusions), subjected to a dilatational line load, for which the solution is known in closed form [26] (not illustrated).

4. Results in the time domain

The displacements and pressures in the spatial–temporal domain are given by a numerical fast Fourier transform in k_z, taking a source whose temporal variation is given by a Ricker wavelet, as defined below. The Ricker wavelet has the advantage of decaying rapidly, in both frequency and time, which both reduces computational effort and allows the computed synthetic waveforms and time series to be interpreted more easily.

The Ricker wavelet function is given by

$$u(\tau) = A(1 - 2\tau^2)\mathrm{e}^{-\tau^2} \tag{5}$$

where A is the amplitude, $\tau = (t - t_s)/t_0$ and t denotes time; t_s is the time when the maximum occurs, while πt_0 is the characteristic (dominant) period of the wavelet. Its Fourier transform is

$$U(\omega) = A\left[2\sqrt{\pi}t_0\mathrm{e}^{-\mathrm{i}\omega t_s}\right]\Omega^2\mathrm{e}^{-\Omega^2} \tag{6}$$

in which $\Omega = \omega t_0/2$.

The Fourier transformations are achieved by discrete summations over wavenumbers and frequencies, which is mathematically the same as adding (virtual) periodic sources at spatial intervals $L = 2\pi/\Delta k_z$ (in the z-axis), and at temporal intervals $T = 2\pi/\Delta\omega$, with Δk_z, and $\Delta\omega$ being the wavenumber and frequency steps, respectively [19]. The spatial separation L must be large enough for the response not to be contaminated by the periodic sources. Thus, the contribution to the response by the fictitious sources must occur at times later than T. A useful mechanism for achieving this is to shift the frequency axis slightly downward, by considering complex frequencies with a small imaginary part of the form $\omega_c = \omega - \mathrm{i}\eta$ (with $\eta = 0.7\Delta\omega$). The periodic sources are thus practically eliminated. In the time domain, this shift is later taken into account by applying an exponential window $\mathrm{e}^{\eta t}$ to the response (see [27]).

5. Numerical applications

The BEM model is used first to compute the seismic response along a homogeneous elastic seabed when its interface is either flat or has smooth deformations. These seabed interface deformations are illustrated and labelled in Fig. 3 as "Interface Type 1" and "Interface Type 2". The first type of deformation is analogous to a smooth ridge, while the second type is analogous to a smooth canyon. The seismic results obtained are compared with the case where the fluid is air, in an attempt to simulate free elastic irregularities. The BEM model is then further extended to accommodate the presence of a buried cylindrical circular water-filled inclusion, below the seabed interface. The axis of this inclusion is placed at $x = 0.0$ m and $y = 90.0$ m (Fig. 3). At time $t = 0.0$ s, a line source, defined by the dilatational potential ϕ, expressed as shown in Eq. (3), acts at the coordinates ($x = 1500.0$ m, $y = 10.0$ m), creating a cylindrical dilatational pulse propagating away from it.

The dilatational wave velocity ($\alpha = 2630$ m/s), the shear wave velocity ($\beta = 1416$ m/s) and density ($\rho = 2250$ kg/m^3) of the elastic medium remain constant in all the analyses. The fluids above the seabed and inside the inclusion are assumed to be water ($\alpha = 1500$ m/s and $\rho = 1000$ kg/m^3), while the fluid above the topographical surface is air ($\alpha = 340$ m/s and $\rho = 1.22$ kg/m^3). Computations are performed in the frequency range (0.25–8.00 Hz), with a frequency increment of 0.25 Hz, which determines the total duration ($T = 4.0$ s) of the analysis in the time domain. The source time-dependence is a Ricker wavelet with a characteristic frequency of 2.5 Hz.

The field generated is computed at three lines of 81 receivers, spaced at equal distances (5.0 m) apart. Two lines of receivers are placed horizontally 1.0 m below and above the seabed surface (lines 1 and 2), while the third is placed vertically in the elastic seabed medium, at $x = -200.0$ m (line 3).

The surface of the seabed and the fluid-filled inclusions are modeled with a number of boundary elements that changes with the excitation frequency of the harmonic load. The ratio between the wavelength of the incident waves and the length of the boundary elements is kept to a minimum of 12. Given the small distance between the horizontal line of receivers and the seabed surface (1.0 m), the length of boundary elements modeling the seabed surface in the vicinity of the line of receivers is at least 0.3 times less than the referenced distance (1.0 m). In any case the number of the boundary elements used to model the surface and the fluid-filled inclusion, is never less than 258 and 32, respectively.

Simulations are performed for different apparent wave velocities along the z-axis to quantitatively study

the 3D effects of the response. The apparent wave velocity (c) results from waves arriving at the z-axis with a path inclination given by $\arccos(v/c)$, where v is the true wave velocity (see Fig. 4).

In Eqs. (2) and (3), presented above, k_z is taken to be ω/c. In the examples selected, two apparent velocities (c) are chosen, namely, $c = \infty$ m/s and $c = 2630$ m/s. Waves arriving at the receivers with a 90° inclination in relation to the z-axis are represented by $c = \infty$ m/s, which can be understood as a pure two-dimensional problem where the source is linear. As the path inclination ranges from 90° to 0°, there is a lower bound value for c that corresponds to the slowest wave velocities (guided waves). Below this value, there are inhomogeneous waves, which decay very quickly with decreasing values of c.

5.1. 2D seabed surface deformations free of any buried inclusion

Fig. 5a and b, respectively, display the amplitude of the total horizontal and the vertical displacement time responses recorded at receivers placed along line 1 for the three seabed surfaces analyzed. These time plots have solid lines indicating the limits of the seabed deformations, to allow an easier interpretation of the results. As expected, the first set of pulses recorded at the receivers corresponds to the incident P wave field and the P and S waves reflected from the surface (labeled PP and PS). Given the small distance between the receiver and surface, only one pulse is visible. The second arrivals are guided waves (G) that travel along the solid–fluid interface. The different pulses are identified in this figure with the labels P, PP, PS and G. The predictions given by ray acoustics are consistent with the arrival times obtained for the different pulses.

Fig. 5 shows that the amplitudes of the displacements generated by guided waves are higher than those generated by the body waves. As expected, the amplitudes of the vertical displacements in the time domain, generated by the guided waves, are higher than the amplitudes of the horizontal displacements, given the elliptical particle motion associated with these waves (see [28]).

Comparing the responses when the flat seabed surface suffers a smooth deformation it can be observed that the major differences are in the horizontal displacements for the pulses generated by the guided waves. The amplification and de-amplification of the response is quite distinct, for the type 1 and type 2 interfaces, respectively. This amplification/de-amplification would be greater if the deformation of the seabed surface was less smooth or if the excitation frequency was higher. The vertical displacements in the time domain for the three seabeds analyzed are similar (Fig. 5b). However, the interface deformations give rise to additional pulses with smaller amplitudes, resulting from the reflection of the guided waves, noticeable particularly at the receivers localized on the source side. These additional pulses would be more visible if the receivers were placed further from the interface deformations.

Fig. 5c displays the amplitude of the pressure responses in the time domain, recorded at receivers placed along line 2 for the three seabed surfaces analyzed. Again, the amplitudes of the pressure responses in the time domain, originated by the guided waves are higher than those originated by the body waves, and the

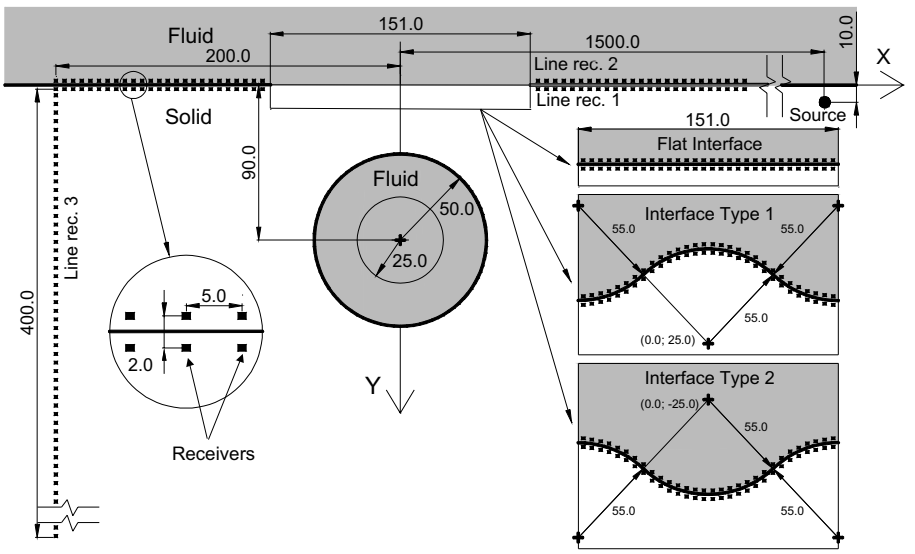

Fig. 3. Geometry of the model used in the numerical applications.

amplification/de-amplification of the pressure waves induced by the seabed interface deformations are visible. However, the type 1 interface now causes a fall in pressure amplitude, while the type 2 interface gives rise to pressure amplitude amplification. Thus, the amplification of the response occurs in the concave part of the solid–fluid interface, while the de-amplification occurs in the convex part of that interface, in relation to the solid medium. In these time plots, only the major amplifications/de-amplifications of the response, occurring at the receivers placed on the central concave/convex part of the seabed surface deformations are visible. If the scale of the plots were changed, minor amplifications/de-amplifications of the response occurring at the receivers placed on the lateral zone of the seabed surface deformations would also be visible.

Fig. 6 shows the Fourier spectra amplitude of the horizontal displacements, recorded along line1 of the receivers, for the geometries of the seabeds analyzed. These plots include lines indicating the limits of the seabed deformations and their inflection points (locating the change of curvature from convex to concave), to allow an easier interpretation of the results. The analyses of these results reveal a significant interference, caused by the seabed's surface deformations, that increases with frequency and is recorded mainly at the receivers located near these deformations. For the type 1 interface the amplification is located in the concave part, while for the type 2 interface signal de-amplification is clearly perceived in the central (convex) part of deformation. The amplification occurs in this case (type 2 interface) at the extremity of the seabed deformation, again in the concave parts of the interfaces. As expected, the amplification is higher at the edge nearer to the source. Also as expected, these Fourier spectra results agree with the time responses (Fig. 5a).

Fig. 7 shows the pressure time responses in line 2 of receivers when the water is replaced by air, for the three solid–fluid interfaces analyzed, in an attempt to compare the results for an irregular seabed with those provided by topographic deformations. These pressure values are much smaller than those obtained for the water (Fig. 5c). This was anticipated, given the higher solid–fluid interaction for the water case, allowing the elastic medium to transfer more energy to the water along its solid–fluid interface. As before, the irregularities in the elastic surface lead to the formation of additional pulses generated by both guided and body waves. This phenomenon is not as visible when the fluid is water (Fig. 5c). One possible reason may be the huge pressure values in the water generated by the guided waves, which mask any slight change in the time response. For both the fluids analyzed, the deformations in the solid–fluid interface lead to a major de-amplification (type 1 interface) and a major amplification (type 2 interface) of the time pressure responses recorded at the receivers in the vicinity of the central part of these deformations; that is, the de-amplifications and amplifications in the convex and concave part of the interface deformation, respectively. In these time plots (Fig. 7), besides the major amplifications/de-amplifications of the response, the minor amplifications/de-amplifications of the response occurring at the receivers placed on the lateral side of the aforementioned surface deformations are also visible.

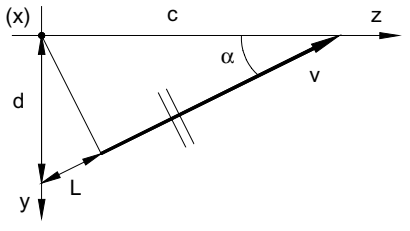

Fig. 4. Apparent wave velocity.

Fig. 8 displays the horizontal displacement in the time domain recorded at the vertical line of receivers (line 3), for the three seabed surfaces modeled. This figure shows that the separation of the different waves P, PP and the PS waves occurs as the depth of receivers increases. As expected, the guided waves' responses exhibit an exponential attenuation of the amplitude as the depth increases, and a phase change at a certain distance from the solid–fluid interface.

Fig. 9 displays the amplitude of the horizontal time displacements for the three solid–fluid interfaces analyzed, when the water is replaced by air. These results show that the time responses exhibit similar features to those found above. It can be seen that there is a slight delay in the arrival time of the guided pulses when the fluid is water.

Comparing the responses for the two fluids analyzed, it can be seen that the phase change occurs at a greater depth when the fluid is air, rather than water. For a homogeneous elastic half-space, the depth where the phase change occurs would be given by $1/(2\pi)$ of the wavelength [28], that is 83.6 m. For the flat seabed, the velocity of the guided waves decreases (see Figs. 8 and 9), leading to a decrease in the wavelength and an (expected) decrease in the depth where the phase change happens. The results for the seabed, given in (Fig. 8), show that the depth where this phase change happens is 51.0 m. When the fluid is air (Fig. 9), the depth obtained for the phase change is 81.0 m, greater than when water is the fluid (seabed), and slightly less than for the half-space case (83.6 m).

The amplitude of the vertical time displacements originated by the guided waves and recorded at receivers placed near the solid–fluid interface, is bigger when the fluid is water (not illustrated).

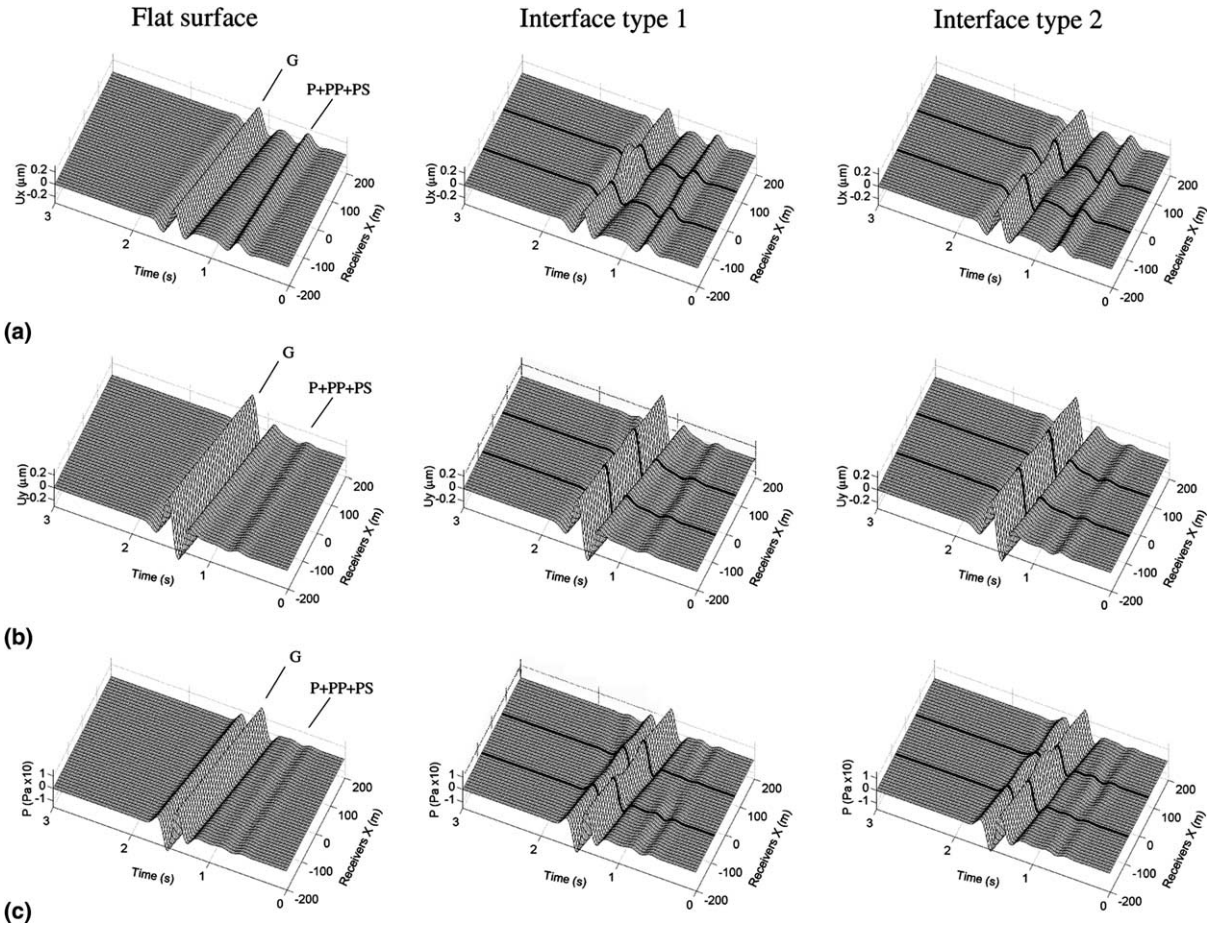

Fig. 5. Responses in the time domain ($c = \infty$ m/s) recorded at receivers placed along: (a) line 1—horizontal displacements; (b) line 1—vertical displacements; (c) line 2—pressure.

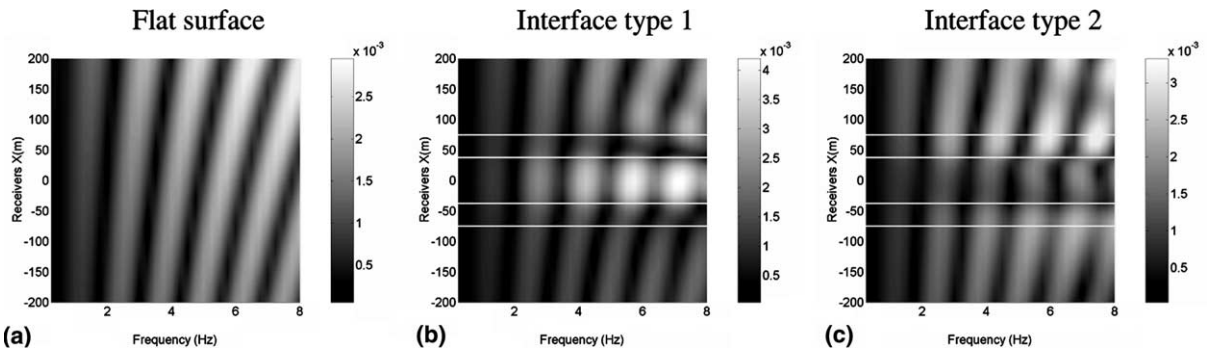

Fig. 6. Fourier spectra ($c = \infty$ m/s) recorded at receivers placed along line 1—horizontal displacements.

5.2. Water-filled inclusions below the 2D seabed surface deformations

This section presents the results obtained when a cylindrical circular water-filled inclusion is buried below the seabed surface. The seismic response is again recorded at the same three lines of receivers and the medium is excited by the same source, placed in the same position.

The horizontal and vertical seismic time displacements, recorded at receiver line 1, when a cylindrical

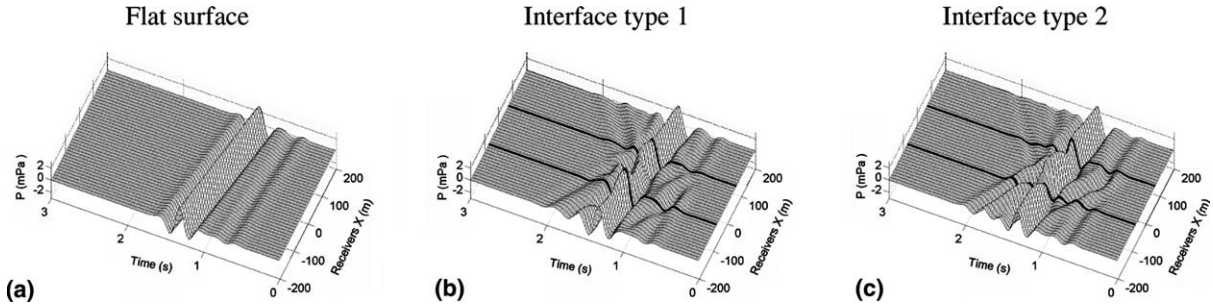

Fig. 7. Responses in the time domain for pressure ($c = \infty$ m/s) recorded at receivers placed along line 2 when the water is replaced by air.

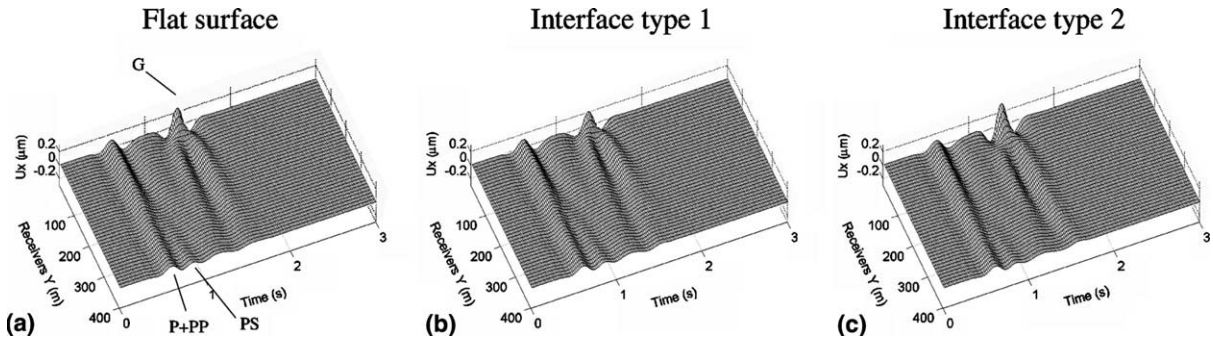

Fig. 8. Responses in the time domain ($c = \infty$ m/s) recorded at receivers placed along line 3—horizontal displacements.

circular fluid-filled inclusion with a radius of 50.0 m is placed under the three seabed surfaces considered, are represented in Fig. 10a and b. The axis of this inclusion is parallel to the seabed surface at $x = 0.0$ m and $y = 90.0$ m , as illustrated in Fig. 3.

Analysis of the results for the horizontal time displacements (Fig. 10a), reveals that there is an important additional time pulse originated by the guided waves traveling around the water-filled inclusion. The amplification and de-amplification of the seismic response is visible. As expected, the larger amplifications are located at the receivers placed on the source side, and the de-amplification, or shadow, was recorded on the other side. When the seabed has a type 1 surface deformation, the major amplification of the horizontal displacements is now registered at the receivers placed above the inclusion (near the interface deformation). If the seabed has a type 2 surface deformation, the major de-amplification occurs at the central receivers, while major amplification occurs at the receivers placed in the source flank side.

The insertion of a fluid-filled inclusion also leads to the appearance of additional pulses and the amplification of the vertical time displacements (Fig. 10b). However, this amplification is now registered at the receivers located above the inclusion. This could be explained by the multiple reflections occurring between the inclusion and the seabed surface, which are polarized vertically. The vertical time displacements originated by the type 1 seabed deformation, exhibit similar features. However, for the type 2 seabed deformation, there is a huge amplification response registered at the central receivers. Again, this could be explained by the multiple reflections between the inclusion and the seabed surface, which is now closer to the inclusion owing to its surface deformation, leading to a higher amplification of the response.

Fig. 10c shows the pressure time response, recorded at receiver line 2. Again, the amplitude of the time pressure responses caused by the guided waves is higher than those originated by the body waves. Comparing Figs. 10c and 5c can be seen that the changes in the time pressure responses due to the insertion of the fluid-filled inclusion in the elastic seabed are greater than those caused by either of the two surface-type deformations.

When the radius of the cylindrical circular water-filled inclusion decreases from 50.0 to 25.0 m the response pattern remain the same. However these patterns, that is, the additional reflected pulses and the amplification/de-amplification of the response, are less pronounced (not illustrated).

Fig. 11 displays the horizontal displacement in the time domain recorded at the vertical line of receivers (line 3), when a water-filled inclusion with a 50.0 m

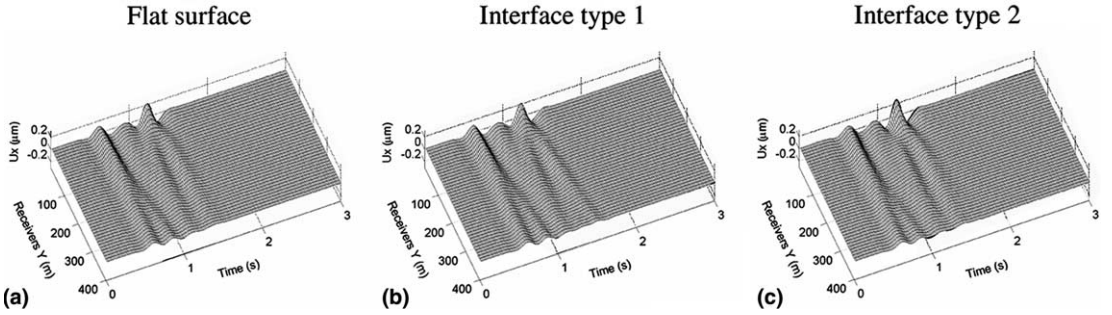

Fig. 9. Responses in the time domain ($c = \infty$ m/s) recorded at receivers placed along line 3—horizontal displacements—when the water is replaced by air.

radius is placed under the three seabed surfaces modeled. For the different body waves (P, PP and PS) the features observed are similar to those observed before (Fig. 8). However, the water-filled inclusion leads to important changes in the guided waves response. The attenuation of the response with the depth is now very low, and the additional scattered field originated by the inclusion apparently disturbs the phase change of the horizontal displacements with the depth. Again, the time responses recorded at the vertical line of receivers are similar for the three seabeds analyzed, leading to the conclusion that the major changes in the seismic

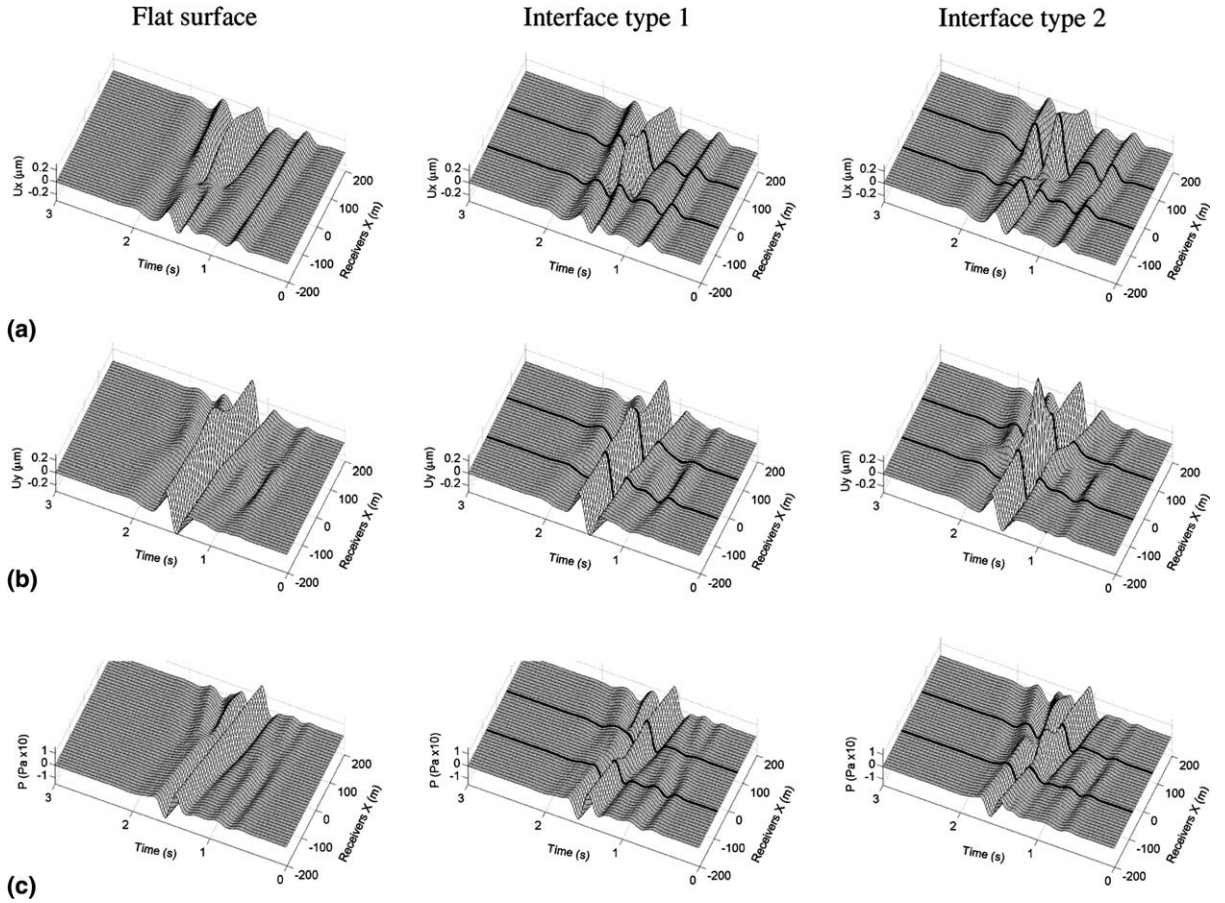

Fig. 10. Responses in the time domain ($c = \infty$ m/s) recorded at receivers placed along: (a) line 1—horizontal displacements; (b) line 1—vertical displacements; (c) line 2—water pressure, when a water-filled inclusion of 50.0 m radius is driven below the seabed surface.

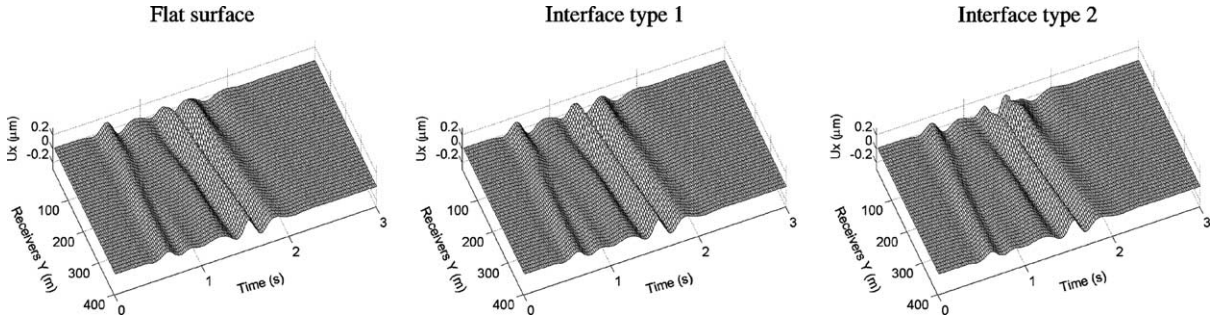

Fig. 11. Responses in the time domain ($c = \infty$ m/s) recorded at receivers placed along line 3—horizontal displacements—when a water-filled inclusion of 50.0 m radius is driven below the seabed surface.

response originated by the seabed surface deformations are localized near the seabed surface.

Numerical simulations were performed for different apparent wave velocities along the z-axis. The results already given in this work correspond to a pure two-dimensional problem (infinite apparent wave velocity). The results illustrated in Fig. 12 were obtained for an apparent wave velocity equal to the P wave velocity (2630 m/s).

Fig. 12a illustrate the z-displacements in the time domain, recorded at the horizontal line of receivers, for a flat seabed surface, both when there is no inclusion, and in the presence of a 25.0 m and 50.0 m radius water-filled inclusion. Without an inclusion, the guided waves are the only pulses that remain clearly visible in the time responses. When there is a water-filled inclusion under the seabed surface, the multi-interactions between pulses reflected from the seabed interface and from the inclusion can be seen; this activity increases when the radius of the inclusion changes from 25.0 to 50.0 m.

The z-displacements recorded at the vertical line of receivers (line 3) are plotted in Fig. 12b. When there is no inclusion, the phase change and the attenuation of the z-displacements that occur with the increase of the depth, are well illustrated. The amplitude of the guided waves on the surface is very high, as expected. Again, the existence of the water-filled inclusion leads to important changes in the pulses originated by the guided waves: an amplification of the displacements and a less pronounced attenuation with increasing depth.

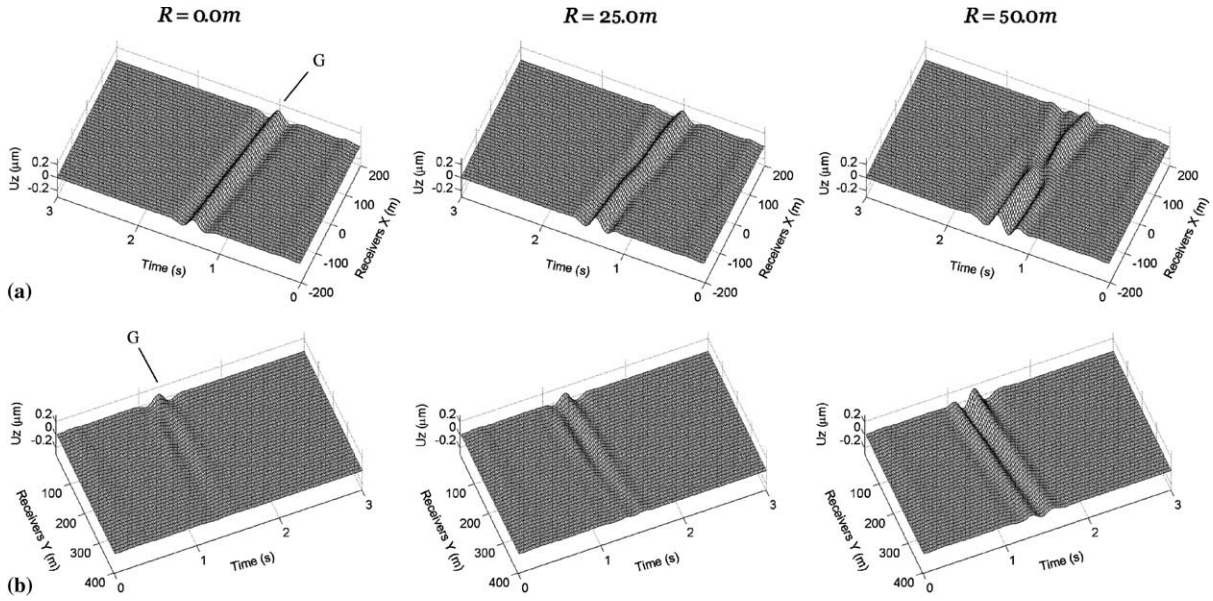

Fig. 12. Responses in the time domain ($c = 2630$ m/s) recorded at receivers placed along: (a) line 1—z-displacements, (b) line 3—z-displacements.

6. Conclusions

The scattering of seismic waves generated by an irregular elastic seabed was evaluated using the Boundary Element Method. The seismic wave field was generated by a dilatational line source, which excites the surrounding medium, creating cylindrical waves that follow different apparent velocities along the z-axis. The responses were analyzed both in time and frequency. As expected, the guided waves dominate the responses recorded at receivers placed near the seabed surface.

The deformation of the seabed surface leads to an amplification and de-amplification of the responses in the concave and convex part of the above-mentioned surface deformations, respectively. This was found for both displacements and pressure responses. In addition to these changes in the amplitude of the response, the seabed surface deformations also give rise to additional scattered pulses.

The importance of the solid–fluid interaction in the seismic response along the solid–fluid interface was analyzed by replacing water by air. The wave field pattern was similar for both fluids, but there is a slight delay in the seismic response when the fluid is water. The depth at which the phase change of the horizontal displacements occurs increases when the fluid is air instead of water. The pressure values recorded at the receivers placed in the water near the solid–fluid interface are much higher than those obtained for the air.

The existence of a water-filled inclusion under the seabed surface leads to important changes in the seismic response, besides the additional pulses and the amplification/de-amplification of the response. The inclusion disturbs the phase change and the attenuation of the guided waves' horizontal displacements. These two features may be related and could be caused by the increased amount of seismic energy that is redirected by the interaction of the inclusion with the seabed interface.

For the seismic waves that result from a dilatational line source, and that have different apparent wave velocities in relation to the z-axis, the features observed were similar, particularly in terms of the attenuation and phase change of the z-displacements of the guided waves with the depth.

References

[1] Wong HL, Trifunac MD. Surface motion of semi-elliptical alluvial valley for incident plane SH-waves. Bull Seism Soc Am 1974;64:1389–403.

[2] Lee VW, Karl JA. Diffraction of SV waves by underground circular cylindrical cavities. Soil Dyn Earthquake Eng 1992;11:445–56.

[3] Sanchez-Sesma FJ. Diffraction of elastic waves by three dimensional surface irregularities. Bull Seism Soc Am 1983;73:1621–36.

[4] Moeen-Vaziri N, Trifunac MD. Scattering and diffraction of plane P and SV waves by two-dimensional inhomogeneities: Part II. Soil Dyn Earthquake Eng 1988;7:189–200.

[5] Lee VW, Wu X. Application of the weighted residual method to diffraction by 2-D canyons of arbitrary shape: II. Incident P, SV and Rayleigh waves. Soil Dyn Earthquake Eng 1994;13:365–75.

[6] Ellis EA, Springman SM. Modelling of soil–structure interaction for a piled bridge abutment in plane strain FEM analyses. Comput Geotech 2001;28(2):79–98.

[7] Yerl HR, Kacin S, Kocak S. A parallel finite–infinite element model for two-dimensional soil–structure interaction problems. Soil Dyn Earthquake Eng 2003;23(4):249–53.

[8] Ohtsuki A, Harumi K. Effect of topography and subsurface inhomogeneities on seismic SV waves. Int J Earthquake Eng Struct Dyn 1983;11:441–62.

[9] Stamos AA, Beskos DE. 3-D seismic response analysis of long lined tunnels in half-space. Soil Dyn Earthquake Eng 1996;15:111–8.

[10] Pedersen HA, Sánchez-Sesma FJ, Campillo M. Three-dimensional Scattering by two-dimensional topographies. Bull Seism Soc Am 1994;84:1169–83.

[11] Santos P, António J, Tadeu A. Wave scattering by 2D smooth topographical elastic deformations caused by a point blast source. Comput Model Eng Sci 2000;1(4):79–98.

[12] Tadeu A, Santos P, António J. Amplification of elastic waves due to a point source in the presence of complex surface topography. Comput Struct 2001;79:1697–712.

[13] Semblat JF, Duval AM, Dangla P. Numerical analysis of seismic wave amplification in Nice (France) and comparisons with experiments. Soil Dyn Earthquake Eng 2000;19:347–62.

[14] Dineva P, Manolis G. Scattering of seismic waves by cracks in multi-layered geological regions II. Numerical results. Soil Dyn Earthquake Eng 2001;21:627–41.

[15] Dawson TW, Fawcett JA. A boundary integral equation method for acoustic scattering in a waveguide with nonplanar surfaces. J Acoust Soc Am 1990;87:1110–25.

[16] Godinho L, Tadeu A, Branco F. 3D acoustic scattering from an irregular fluid waveguide via the BEM. Eng Anal Boundary Elements 2001;25:443–53.

[17] Ingenito F. Scattering from an object in a stratified medium. J Acoust Soc Am 1987;82(6):2051–6.

[18] Makris NC. A spectral approach to 3D object scattering in layered media applied to scattering from submerged spheres. J Acoust Soc Am 1998;104(4):2105–13.

[19] Bouchon M, Aki K. Discrete wave-number representation of seismic-source wave field. Bull Seism Soc Am 1977;67:259–77.

[20] Beskos DE. Boundary element methods in dynamic analysis: Part II (1986–1996). Appl Mech Rev 1997;50(3):149–97.

[21] Brebbia CA, Telles JCF, Wrobel LC. Boundary element technique. Springer-Verlag; 1984.

[22] Tadeu A, Godinho L, Santos P. Wave motion between two fluid filled boreholes in an elastic medium. Eng Anal Boundary Elements 2002;26:101–17.

[23] Tadeu A, Santos P, Kausel E. Closed-form integration of singular terms for constant, linear and quadratic boundary

elements—Part I: SH wave propagation. Eng Anal Boundary Elements 1999;23(8):671–81.
[24] Tadeu A, Santos P, Kausel E. Closed-form integration of singular terms for constant, linear and quadratic boundary elements—Part II: SV–P wave propagation. Eng Anal Boundary Elements 1999;23(9):757–68.
[25] Pao YH, Mow CC. Diffraction of elastic waves and dynamic stress concentrations. Rand Corporation; 1973.
[26] Tadeu A, António J. 2.5D Green's functions for elastodynamic problems in layered acoustic and elastic formations. J Comput Model Eng Sci 2001;2(4):477–95.
[27] Kausel E, Roesset JM. Frequency domain analysis of undamped systems. J Eng Mech-ASCE 1992;118(4):721–34.
[28] Richart FE, Wood RD, Hall JR. Vibration of soils and foundations. New Jersey: Prentice-Hall; 1970.